A spectrally composite reconstruction approach for improved resolution of pulsed photothermal temperature profiling in water-based samples

2009 Phys. Med. Biol. 54 2829

(http://iopscience.iop.org/0031-9155/54/9/016)

IOP PUBLISHING PHYSICS IN MEDICINE AND BIOLOGY

Phys. Med. Biol. **54** (2009) 2829–2844 doi:10.1088/0031-9155/54/9/016

A spectrally composite reconstruction approach for improved resolution of pulsed photothermal temperature profiling in water-based samples

Matija Milanič, Igor Serša and Boris Majaron

Jožef Stefan Institute, Jamova 39, SI 1000 Ljubljana, Slovenia

E-mail: matija.milanic@ijs.si, igor.serša@ijs.si and boris.majaron@ijs.si

Received 11 September 2008, in final form 13 March 2009
Published 15 April 2009
Online at stacks.iop.org/PMB/54/2829

Abstract

We report on the first experimental evaluation of pulsed photothermal radiometry (PPTR) using a spectrally composite kernel matrix in signal analysis. Numerical studies have indicated that this approach could enable PPTR temperature profiling in watery tissues with better accuracy and stability as compared to the customary monochromatic approximation. By using an optimized experimental set-up and image reconstruction code (involving a projected ν-method and adaptive regularization), we demonstrate accurate localization of thin absorbing layers in agar tissue phantoms with pronounced spectral variation of a mid-infrared absorption coefficient. Moreover, the widths of reconstructed temperature peaks reach 14–17% of their depth, significantly less than in earlier reports on PPTR depth profiling in watery tissues. Experimental results are replicated by a detailed numerical simulation, which enables analysis of the broadening effect as a function of temperature profile amplitude and depth.

(Some figures in this article are in colour only in the electronic version)

1. Introduction

Pulsed photothermal radiometry (PPTR) enables the reconstruction of temperature depth profiles induced by pulsed laser exposure of a sample from the resulting transient change in mid-infrared (IR) emission (Long *et al* 1987). As a promising modality for non-invasive determination of subsurface chromophore distribution in biological tissues, PPTR temperature profiling was intensively investigated (e.g., Jacques *et al* 1993, Bindra *et al* 1994, Milner *et al* 1995, Vitkin *et al* 1995, Milner *et al* 1996, Sathyam and Prahl 1997, Smithies *et al* 1998, Majaron *et al* 2000, 2002, Choi *et al* 2004a). In addition to structural information (and unlike competing imaging modalities), PPTR can also provide the actual temperature values. Access

to both types of information on an individual patient basis could significantly improve the efficacy and safety of medical laser applications, especially in dermatology (van Gemert *et al* 1997, Verkruysse *et al* 2000).

Various groups have found that PPTR temperature profiling is fairly efficient at determining the depth of subsurface absorbing layers (Milner *et al* 1995, Sathyam and Prahl 1997, Milanič *et al* 2007). However, the main limitation of this technique is a significant broadening (and attenuation) of distinct temperature peaks. This artifact increases with object depth, essentially limiting the usable depth of PPTR temperature profiling. Sathyam and Prahl (1997) reported a broadening equal to 50–60% of the object depth. The results by Smithies *et al* (1998) indicate a smaller broadening (∼25% of the depth), but only in an oversimplified numerical simulation. After further development of this approach (e.g., Majaron and Milanič 2007, 2008), measurements in agar tissue phantoms showed reconstructed temperature profiles with the widths equal to 19–28% (Milanič *et al* 2007) and 11–36% of the absorber depth (Milanič *et al* 2008). However, these widths included an uncontrolled actual thickness of the absorption layer. In addition, the observed widths were affected by the non-uniformity of absorption layer depth within the signal acquisition area, and thus, may not reflect the ultimate depth resolution of PPTR depth profiling. To the best of our knowledge, temperature profile reconstruction in all earlier experimental studies was performed within the so-called monochromatic approximation (Majaron *et al* 2002). In watery tissues, this approach requires a careful selection of the effective IR absorption coefficient (Majaron and Milanič 2008) and narrowing of the acquisition spectral range, at the expense of the reduced signal-to-noise ratio (Majaron *et al* 2007, 2008). In the present study, we utilize the entire spectral range of the InSb radiation detector ($\lambda = 3.0$–$5.6\ \mu$m) and apply a spectrally composite kernel matrix in the reconstruction process, which leads to more accurate profiling in a numerical simulation (Majaron and Milanič 2007). In addition, we use an optimized experimental set-up and updated image reconstruction code.

Systematic measurements of PPTR temperature profiling accuracy and axial resolution are performed in agar tissue phantoms with optimized, better-controlled structure. The depths of absorbing layers are determined independently by high-resolution magnetic resonance imaging (MRI).

The experimental results are supported by a detailed numerical simulation of the procedure, involving noise with amplitude and spectral characteristics consistent with experimental data. In addition, we simulate imaging of δ-profiles to assess the net broadening effect and analyze its dependence on temperature profile amplitude and depth.

2. Materials and methods

2.1. Theoretical background

Basic relations of PPTR temperature profiling were derived earlier (e.g., Milner *et al* 1995, Sathyam and Prahl 1997, Majaron *et al* 2002). In summary, the radiometric transient following pulsed laser irradiation of a sample can be expressed in a monochromatic approximation as

$$\Delta S_\lambda(t) = C\,B'_\lambda(T_b)\mu_{\mathrm{IR}} \int_{z'=0}^{\infty} \Delta T(z',0) \int_{z=0}^{\infty} K_{\mathrm{T}}(z',z,t)\ \mathrm{e}^{-\mu_{\mathrm{IR}} z}\ \mathrm{d}z\ \mathrm{d}z', \qquad (1)$$

where constant C accounts for specifics of the sample surface, collection optics and radiation detector, $B'_\lambda(T_0)$ denotes the derivative of Planck's radiation formula with respect to temperature (expressed at baseline temperature T_b) and $K_{\mathrm{T}}(z', z, t)$ stands for thermal Green's

function. Since none of these vary with the initial temperature profile $\Delta T(z', 0)$, the latter is related to $\Delta S_\lambda(t)$ by a simple convolution:

$$\Delta S_\lambda(t) = \int_{z=0}^{\infty} K_\lambda(z, t)\ \Delta T(z, 0)\, \mathrm{d}z. \tag{2}$$

For a semi-infinite medium with convective and/or radiative heat transfer at the surface, the monochromatic kernel function $K_\lambda(z, t)$ was derived by Milner *et al* (1995):

$$K_\lambda(z, t) = \frac{1}{2} C\ B'_\lambda(T_b)\mu_{\mathrm{IR}} \exp[-z^2/(4Dt)] \times \left\{ \mathrm{erfcx}(u_-) + \mathrm{erfcx}(u_+) + \frac{2h}{(\mu_{\mathrm{IR}} - h)} [\mathrm{erfcx}(u_+) - \mathrm{erfcx}(u_1)] \right\}, \tag{3}$$

where $\mathrm{erfcx}(u) = [1 - \mathrm{erf}(u)]\ \exp(u^2)$, $u_\pm = \mu_{\mathrm{IR}}\sqrt{Dt} \pm z'/(2\sqrt{Dt})$ and $u_1 = h\sqrt{Dt} + z'/(2\sqrt{Dt})$. The reduced heat transfer coefficient, h, is defined as the ratio between the customary heat transfer coefficient at the interface (in W m^{-2} K^{-1}) and thermal conductivity of the sample, and D marks its thermal diffusivity.

To account for the spectral variation of μ_{IR} within a broad detection band (λ_l–λ_h), the theory was extended (Majaron *et al* 2002), resulting in

$$\Delta S(t) = C' \int_{\lambda_l}^{\lambda_h} R(\lambda) \int_{z=0}^{\infty} B'_\lambda(T_b)\Delta T(z, t)\mu_{\mathrm{IR}}(\lambda)\ \mathrm{e}^{-\mu_{\mathrm{IR}}(\lambda)z}\, \mathrm{d}z\ \mathrm{d}\lambda, \tag{4}$$

where $R(\lambda)$ stands for the spectral responsivity of the IR radiation detector. After replacing the temperature field evolution $\Delta T(z, t)$ with the solution given by the Green's approach and following the same arguments as in the monochromatic case, an analogous convolution relation is obtained:

$$\Delta S(t) = \int_{z=0}^{\infty} K(z, t)\ \Delta T(z, 0)\, \mathrm{d}z. \tag{5}$$

The spectrally composite kernel function $K(z,t)$ can easily be derived from (2)–(5).

In all practical applications, the initial temperature profile (object) and the corresponding signal are represented as vectors $\boldsymbol{T}_{\mathrm{obj}} \in \mathrm{R}^{\mathrm{n}}$ and $\boldsymbol{S}_{\mathrm{obj}} \in \mathrm{R}^{\mathrm{m}}$, respectively, which turn (5) into a simple multiplication with kernel matrix $\boldsymbol{K} \in \mathrm{R}^{\mathrm{m}\times\mathrm{n}}$:

$$S_{\mathrm{obj}} = \boldsymbol{K}\boldsymbol{T}_{\mathrm{obj}}; \qquad K_{ij} = K(z_j, t_i)\Delta z. \tag{6}$$

The reconstruction of $\boldsymbol{T}_{\mathrm{obj}}$ from PPTR signals presents a severely ill-posed inverse problem (Milner *et al* 1995). This results primarily from the ill-determined rank of matrix $\boldsymbol{K}$, which prevents the computation of its inverse with sufficient accuracy. Moreover, experimental signals $\boldsymbol{S}$ will include noise, and matrix $\boldsymbol{K}$ may not describe accurately all the involved physical processes. Therefore, the equation $\boldsymbol{S} = \boldsymbol{K}\boldsymbol{T}$ in general does not have a solution $\boldsymbol{T}$, and it is customary to seek an approximate solution by solving the minimization problem

$$\min \|\boldsymbol{S} - \boldsymbol{K}\boldsymbol{T}\|^2. \tag{7}$$

2.2. Layered agar tissue phantoms

Each tissue phantom consisted of a ~2 mm thick agar gel substrate layer, a thin optically absorbing layer and a superficial agar gel layer of constant thickness (figure 1).

Agar gel was prepared by dissolving 0.15 mg of agar powder in 6 ml of distilled water. Polymerization was initiated by heating the mixture to its boiling point in a microwave oven. Each gel layer was produced separately by injecting a suitable amount of the polymerizing agar solution onto a wetted microscope slide with two identical spacers positioned near each end.

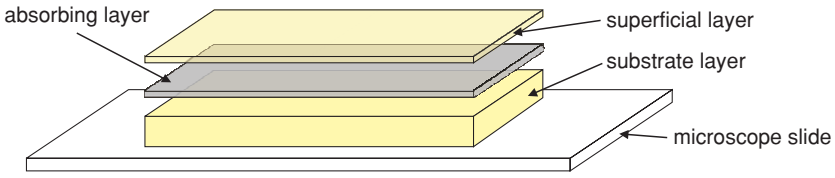

Figure 1. Schematic of a tissue phantom, consisting of a thin absorbing layer sandwiched between two agar gel layers.

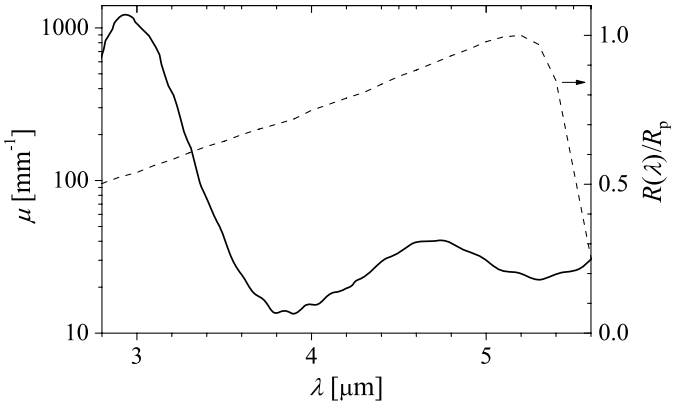

Figure 2. Measured absorption coefficient of the agar gel in the mid-IR spectral range (solid line) and spectral responsivity of the InSb detector, $R(\lambda)$, relative to its peak value, R_p (dashed line).

The use of a syringe prevented the inclusion of air bubbles, which were especially present near the agar solution surface. A second slide was then placed on top of the setting agar layer and pressed against the spacers. When polymerization was complete, the top slide was carefully removed, exposing a gel layer with a uniform thickness and flat, smooth surface.

The absorbing layers consisted of a thin, colored (pink) polyethylene foil, which ensured a controlled and spatially uniform absorption of laser light. Seven tissue phantoms evaluated below (samples A–G) involved very thin absorbing layers (foil thickness $d \sim 7$ μm) and superficial layers with thickness between ∼40 μm and 0.9 mm. Three samples (marked B1–D1), also used for magnetic resonance imaging, featured slightly thicker absorbing layers ($d \sim 30$ μm) at subsurface depths of 0.2–0.5 μm.

All tissue phantoms were constructed in a water bath to prevent the formation of air bubbles between adjacent layers. When necessary, the samples were kept in airtight plastic containers with humid air for a short period of time, before being used in experiments.

2.3. Experimental set-up

Each PPTR measurement involves irradiation of the sample with a single 1 ms pulse from a KTP/Nd:YAG laser at 532 nm. The radiant exposure near the center of a laser spot (diameter ∼7 mm) was approximately 0.24, 0.35, or 0.51 J cm^{-2}. IR radiation emitted from the center of irradiated area was collected by two planoconvex Si lenses (Galvoptics, Essex, UK) positioned for magnification $M = 1$. The lenses were coated for high transmittance ($T \geqslant 98\%$) in the acquisition spectral band of the single-element InSb detector (P5968–100, Hamamatsu; $\lambda =$ 3.0–5.6 μm) with a 1 mm diameter, 45° field of view and peak spectral sensitivity $R_p =$ 2.5 A/W at $\lambda_p = 5.3$ μm (figure 2).

PPTR measurements were performed at three different sites on each sample. The sites were separated by a few millimeters to prevent thermal interference between successive measurements. In samples A–G, a different radiant exposure was used at each measurement site. In samples B1–D1, only the lowest radiant exposure ($H = 0.24$ J cm^{-2}) was applied to minimize the risk of thermal damage.

The radiometric signals were acquired for 1.5 s after the laser pulse, at a rate of 50 000 s^{-1}. The PPTR signals $\boldsymbol{S}$ were obtained by calibrating the raw data using a computer-controlled blackbody (BB701, Omega Engineering, Stamford, CT, USA), subtracting the baseline value and averaging 50 subsequent data points, thus reducing the effective acquisition rate to 1000 s^{-1}.

2.4. Reconstruction of temperature profiles

The spectrally composite kernel matrix $\boldsymbol{K}$ was computed by dividing the acquisition spectral band ($\lambda = 3.0$–5.6 μm) into intervals of width 0.02 μm and adding their contributions (Milanič *et al* 2008):

$$K_{i,j} = \sum_{n=1}^{N} R(\lambda_n)\ B'_{\lambda_n}(T_b)\ \kappa_n(z_j, t_i; \mu_n) \Bigg/ \sum_{n} R(\lambda_n)\ B'_{\lambda_n}(T_b). \tag{8}$$

Here, λ_n is the central wavelength of the nth spectral interval, μ_{n} is the corresponding IR absorption coefficient of the agar gel (figure 2) and $R(\lambda_n)$ is the spectral responsivity of the InSb detector (figure 2). The thermal parameters of agar were estimated to $D = 0.143$ mm^2 s^{-1} and $h = 0.02$ mm^{-1}.

The initial temperature profiles $\boldsymbol{T}$, consisting of 300 equidistant temperature values over a depth range of 1.5 mm, were then reconstructed by solving (7) using the projected ν-method. The ν-method is an iterative minimization approach, derived from the classical Landweber algorithm (Brakhage 1987, Hansen 1998). While the latter has a slower convergence as compared to conjugate gradient (CG) algorithm, the ν-method is significantly accelerated by involving a weighted average of the last two iterates and allowing the weight factors μ and ω to vary with iteration number i (see algorithm 1). The convergence of this method depends on the value of a real constant, $\nu\ \varepsilon$ (0,1). In preliminary tests, we have found that $\nu = 0.99$ works well for our inverse problem. Moreover, the ν-method does not converge for $\|\boldsymbol{K}\|_2 > 1$, and the convergence is fastest for $\|\boldsymbol{K}\|_2$ slightly smaller than 1. Therefore, we have assured convergence by substituting $\boldsymbol{K}$ and $\boldsymbol{S}$ with modified kernel matrix and signal vectors, $\boldsymbol{A}$ and $\boldsymbol{b}$, where ε is a small constant (e.g., $\varepsilon = 10^{-3}$).

Although the laser-induced temperature rise $\boldsymbol{T}_{\mathrm{obj}}$ is inherently non-negative, the ν-method solutions often include unphysical negative values. Based on good experience with the augmentation of CG (Milner 1995, Majaron and Milanič 2007) and singular-value decomposition algorithms (Verkruysse *et al* 2005), we have implemented a non-negativity constraint in the ν-method. We have selected the so-called projection approach, whereby the negative components of unconstrained solution $\boldsymbol{t}_i$ are set to zero in each iteration step (see line 10 in algorithm 1).

In the ν-method, solutions $\boldsymbol{T}_i$ initially approach the correct solution, but often deviate from it in later iteration steps. In order to obtain acceptable solutions $\boldsymbol{T}_{\mathrm{reg}}$, we regularize the iteration by early termination, whereby the step count i serves as the regularization parameter. The optimal degree of regularization is determined by a combination of two stopping criterions, the discrepancy principle (Groetsch 1984) and Monte Carlo generalized cross validation (Girard

1989). Including two stopping criteria improves the robustness of the algorithm and enables automatic adaptation of the code to a wide range of signal-to-noise ratios.

Algorithm 1: The projected ν-method minimizes the expression $\|\boldsymbol{S} - \boldsymbol{KT}\|^2$ for provided matrix $\boldsymbol{K}$ and vector $\boldsymbol{S}$.

$\boldsymbol{A} = \boldsymbol{K}/(\|\boldsymbol{K}\|_2 + \varepsilon)$;
$\boldsymbol{b} = \boldsymbol{S}/(\|\boldsymbol{K}\|_2 + \varepsilon)$;
$i = 1$;
$\mathbf{T}_0 = 0$;
$\boldsymbol{r}_0 = \boldsymbol{b}$;
repeat:
$\mu_i = 1 + (i\text{–}1)(2i\text{–}3)(2i + 2\nu\text{–}1)/[(i + 2\nu\text{–}1)(2i + 4\nu\text{–}1)(2i + 2\nu\text{–}3)]$;
$\omega_i = 4\,(2i + 2\nu\text{–}1)(i + \nu\text{–}1)/[(i + 2\nu\text{–}1)(2i + 4\nu\text{–}1)]$;
$\boldsymbol{t}_i = \mu_i\,\boldsymbol{T}_{\,i-1} + (1\text{–}\mu_i)\,\boldsymbol{T}_{\,i-2} + \omega_i \boldsymbol{A}^{\mathrm{T}} \boldsymbol{r}_{i-1}$;
$\boldsymbol{T}_i = (\boldsymbol{t}_i)^+$;
$\boldsymbol{r}_i = \boldsymbol{b} - \boldsymbol{A}\boldsymbol{T}_i$;
$i = i + 1$;
until(stopping criterion)
$\boldsymbol{T}_{\mathrm{reg}} = \boldsymbol{T}_i$.

Our projected ν-method is implemented in MatLab environment (the MathWorks, Inc.). Matrix elements $K_{i,j}$ are computed with high precision by using the Chebyshev approximation (Cody 1969) to evaluate the exponential complementary error functions erfcx(u) in (3). Special care is also taken to avoid unnecessary matrix multiplications, which greatly reduces the round-up errors.

2.5. Magnetic resonance imaging (MRI)

Our high-resolution MRI system consists of a horizontal-bore superconducting magnet (Oxford, Abingdon, Oxfordshire, UK) producing a 2.35 T magnetic field (proton frequency 100 MHz), a NMR/MRI spectrometer (Apollo, TecMag, Houston, TX) and accessories for MR microscopy with a top gradient of 0.25 T m^{-1} (Bruker, Ettlingen, Germany). A 3D proton-weighted image was produced using a spin-echo technique (echo time 7 ms, repetition time 1000 ms). The imaged volume (16 × 4 × 4 mm) was covered by a 512 × 128 × 128 matrix, yielding an isotropic resolution of 31 μm. Averaging the results from four acquisition sequences resulted in a total imaging time of ∼18 h. The distance between the sample surface and the absorbing layer was determined from vertical cross-sectional images at 10 positions in each sample.

3. Experimental results

PPTR signals acquired from samples A–G at $H = 0.24$ J cm^{-2} are presented in figure 3. The noise-equivalent temperature rise, determined as the standard deviation of radiometric signals before the laser exposure, equals $NE\Delta T = 2.2$ mK. As shown in figure 4, the average signal-to-noise ratio (SNR) decreases approximately exponentially with absorbing layer depth (Z).

Figure 5 presents the statistical analysis of the reconstruction results for samples A–G (see the labels) and three radiant exposures (H). Solid lines connect the average temperatures and gray bars indicate standard deviations. Evidently, temperature profiles broaden with an increasing depth of the absorption layer (Z) for all H. Also, the reconstructed images of all

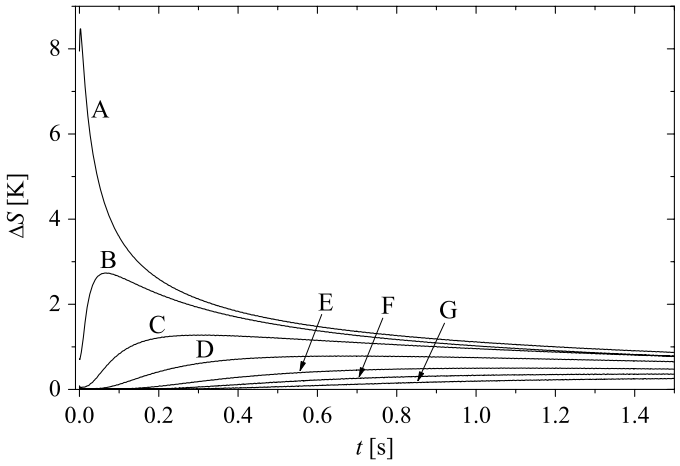

Figure 3. PPTR signals acquired from samples A–G (see the labels) at radiant exposure $H = 0.24$ J cm^{-2}.

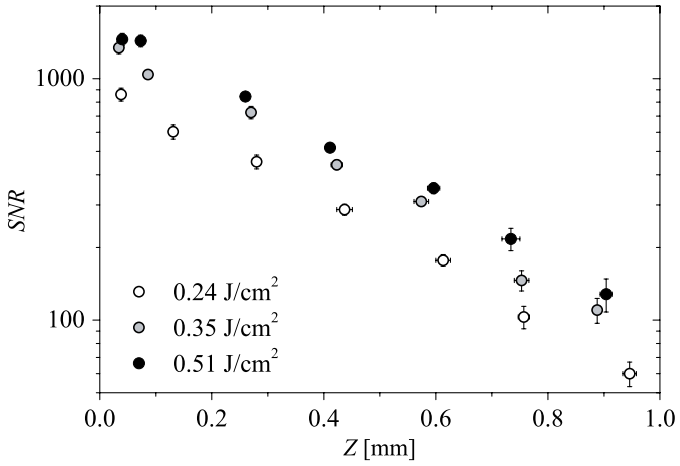

Figure 4. SNR in PPTR signals obtained with different radiant exposures, H (see the legend), applied to tissue phantoms with different absorbing layer depths (Z). The bars are the standard deviations of SNR and Z.

samples are broader for $H = 0.24$ J cm^{-2} (left column) as compared to $H = 0.35$ (center) and 0.51 J cm^{-2} (right). The images of samples B–D feature the largest standard deviations at $H = 0.24$ J cm^{-2} and smallest at $H = 0.51$ J cm^{-2}.

In figure 6, we present the widths of reconstructed temperature profiles as a function of depth Z for samples A–G and radiant exposures $H = 0.24$ J cm^{-2} (left), 0.35 J cm^{-2} (center) and 0.51 J cm^{-2} (right). The widths (W) increase approximately linearly with Z, except at depths below 300 μm where the actual width of the initial temperature profile prevails over the broadening effect. By considering only the results for samples D–G, we find that the width W increases approximately as 17, 14 or 15% of depth Z (for $H = 0.24$, 0.35 and 0.51 J cm^{-2}, respectively). On average, the determined W are 19% larger for $H = 0.24$ J cm^{-2}

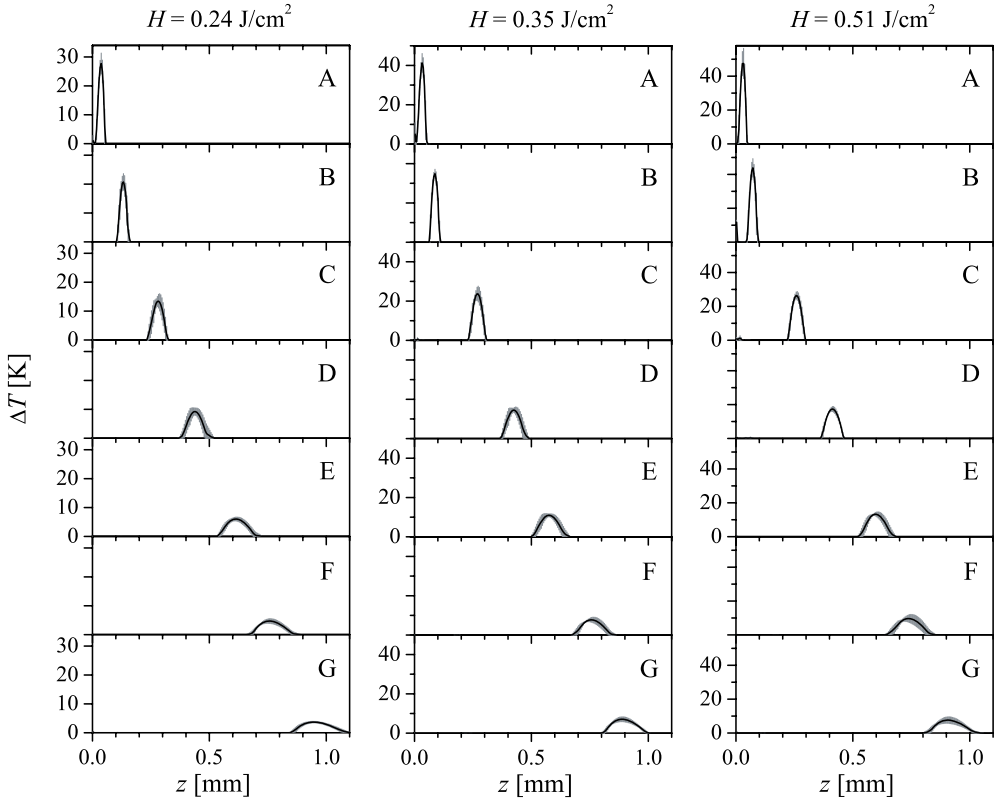

Figure 5. Average temperature profiles (solid lines) and standard deviations (gray bars) reconstructed from ten PPTR signals acquired from samples A–G using radiant exposures $H = 0.24$ J cm^{-2} (left), 0.35 J cm^{-2} (center) and 0.51 J cm^{-2} (right).

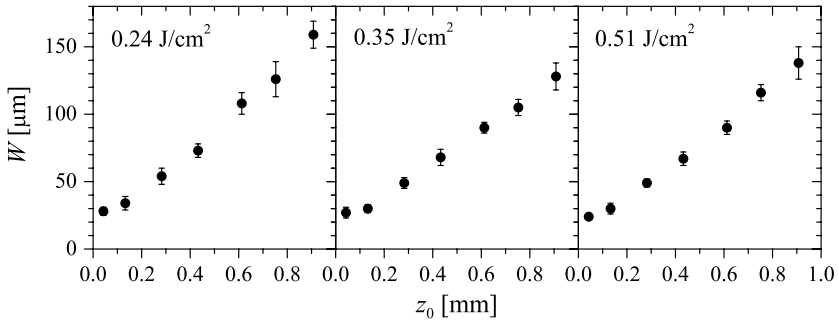

Figure 6. Temperature peak width W as a function of peak temperature depth Z as obtained for samples A–G using three radiant exposure values (see the labels). The bars represent standard deviations.

as compared to 0.35 J cm^{-2}, while differences between the widths for $H = 0.35$ J cm^{-2} and $H = 0.51$ J cm^{-2} are not significant. This shows that H influences the temperature profile widths when H is low, but the effect of H on W is less significant when H is large (i.e., above a certain SNR).

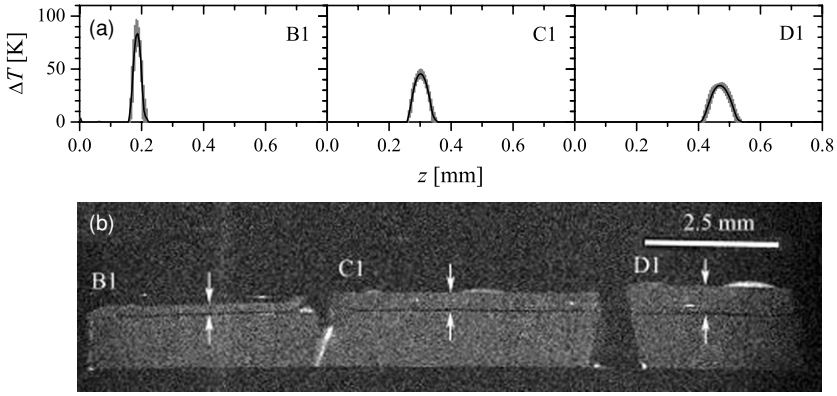

Figure 7. (a) Average temperature profiles (solid lines) and standard deviations (gray bars) reconstructed from ten PPTR signals acquired from samples B1–D1 ($H = 0.24$ J cm^{-2}). (b) MRI cross-sectional image of samples B1 (left), C1 (center) and D1 (right). In each sample, the upper arrows mark the surface and the lower ones the absorbing layer.

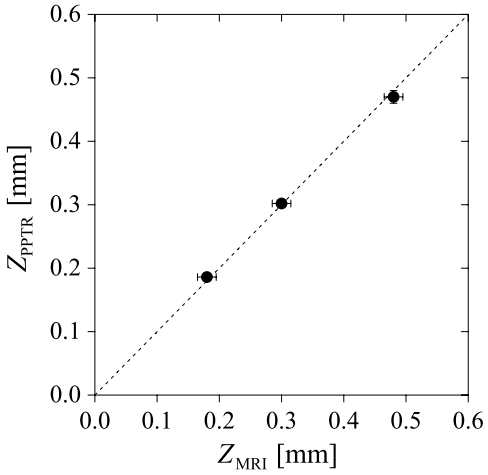

Figure 8. Absorbing layer depth Z as assessed from PPTR and MRI measurements in samples B1–D1; the dashed line represents the ideal match, $Z_{PPTR} = Z_{MRI}$.

We also compare the absorbing layer depths obtained by PPTR profiling with those found by MRI (figure 7). The cross-sectional image of samples B1–D1 clearly shows their surfaces (upper arrows) and absorbing layers (lower arrows). The peak temperatures in figure 7(a) are higher as compared to figure 5, because a thicker absorbing foil was used in samples B1–D1 for improved MRI contrast.

The absorbing layer depths determined from PPTR reconstruction results and MRM agree very well (figure 8). The largest discrepancy ($\sim$10 μm), observed in sample D1, is 3 times smaller than the theoretical resolution of MRI. This proves that the accuracy of the absorbing layer depth determined by PPTR temperature profiling is very high, at least to the depth of $\sim$0.5 mm.

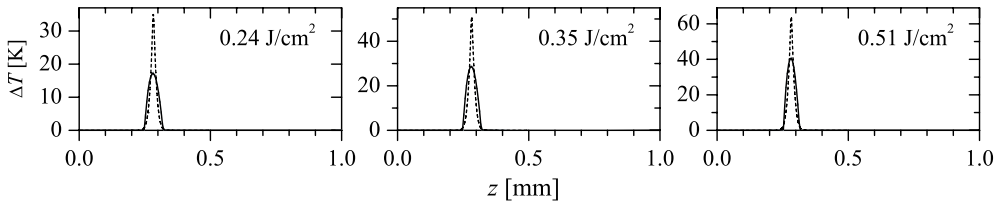

Figure 9. Temperature profiles reconstructed from simulated PPTR signals for test object centered at $z_1 = 282$ μm (dashed line) and three amplitudes representing different radiant exposure values (see the labels).

4. Numerical analysis

4.1. Simulation of experiments

In numerical simulation of our PPTR measurements in test samples A–G, we consider planar, uniformly absorbing layers with a width of 7 μm and subsurface depth (z_1) between 40 and 905 μm. To account for the diffusion of heat from the absorbing layer, the temperature profile at the end of the laser pulse (with duration $t_p = 1$ ms) is calculated as

$$\Delta T(z, 0) = \int_0^\infty \mathrm{d}z' \int_0^{t_\mathrm{p}} s(z', t)\ K_\mathrm{T}(z', z, t_p - t)\,\mathrm{d}t, \tag{9}$$

where $s(z', t)$ is a uniform heat source (in units of K s^{-1}) centered at z_1. To determine the source amplitudes that correspond to experimentally applied radiant exposures, we have computed PPTR signals from $\Delta T(z, 0)$ (9) for two shallowest absorbing layers ($z_1 = 40$ and 130 μm). A comparison between the simulated and experimental PPTR signals indicated that the initial profile amplitudes of 35, 51 and 64 K correspond to the radiant exposures of 0.24, 0.35 and 0.51 J cm^{-2}, respectively.

For additional realism, the PPTR signals $\boldsymbol{S}_0$ computed using (6) were augmented by noise, which included both zero-mean white noise and the so-called $1/f$ noise (Vincent 1989). Based on the analysis of experimental radiometric signals, the total noise amplitude was $NE\Delta T = 2.2$ mK and the $1/f$ noise was characterized by the corner frequency $f_c = 15$ Hz and exponent $\alpha = 1.3$ (Milanič 2008).

The initial temperature profiles $\boldsymbol{T}$ were reconstructed from simulated PPTR signals $\boldsymbol{S}$ using the same spectrally composite kernel matrix $\boldsymbol{K}$ (8) as in the experimental part of this study. The results (figure 9) support our experimental observation that higher radiant exposures lead to narrower temperature profiles. Standard deviations of the temperature values, determined from 30 examples with different noise realizations, are also plotted (gray vertical bars), but are too small to be observed.

Temperature peak widths W are plotted in figure 10 as a function of test objects depth z_0 for all radiant exposure values. Evidently, the widths obtained in numerical simulations (open circles) match our experimental data (samples A–G; solid circles) within their respective uncertainties.

Figure 11 compares the reconstructed peak temperature depths (Z) with the centers of initial temperature profiles (z_0). At $H = 0.24$ J cm^{-2} (left panel), the values Z are practically equal to z_0 for test objects A–D ($z_0 < 0.5$ mm), and approximately 1% smaller for deeper absorbing layers. Very similar results were obtained for $H = 0.35$ and 0.51 J cm^{-2} (right). This shows that even in the presence of realistic noise, the PPTR determined depth of a thin absorbing layer can be very accurate.

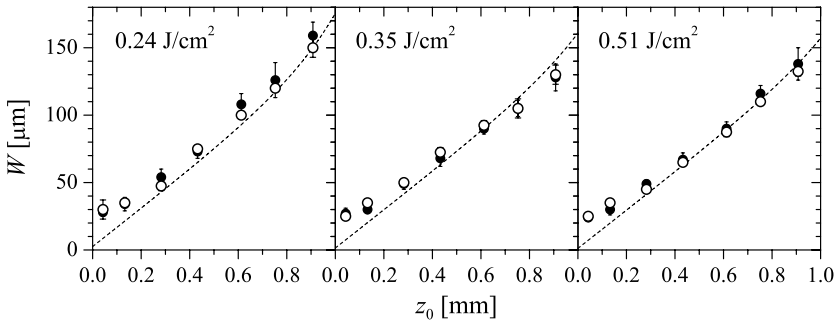

Figure 10. Temperature peak width (W) in depth profiles reconstructed from simulated (open circles) and experimental PPTR signals (solid circles) as a function of absorber depth z_0 for three radiant exposures (see the labels). Dashed lines represent the broadening model function $w(z_0, a)$ (11).

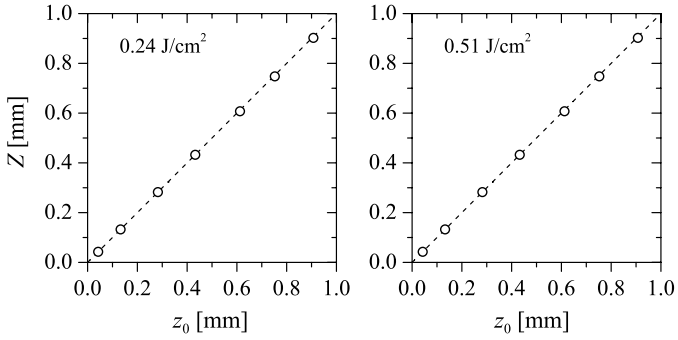

Figure 11. Peak temperature depths Z from reconstructed images of simulated test objects A–G versus the actual central depths z_0 for two radiant exposures (see the labels). Dashed lines indicate a perfect match (i.e., $Z = z_0$).

4.2. Broadening of delta profiles

The width of the reconstructed temperature peak is always a combination of the actual temperature profile and broadening due to inherent limitations of the PPTR profiling process. In order to isolate the latter, we consider in the following infinitely narrow temperature profiles, i.e., delta functions, $\Delta T(z, 0) = a\,\delta(z - z_0)$. Substituting this into (5) yields the corresponding PPTR signal

$$\Delta S\,(t) = a\;K\;(z_0, t)\,. \tag{10}$$

Theoretical signal vectors $\boldsymbol{S}_0$ computed using (10) with kernel matrix $\boldsymbol{K}$ (8) were augmented with realistic noise, just as in the previous section. By varying the amplitude a between 0.15 and 1.95 mm K, we have covered the range of SNR values as observed in the experiments (figure 12).

Figure 13 presents statistical analysis of 30 reconstruction results for δ-function located at $z_0 = 0.273$ mm (similar to sample C) and amplitude $a = 0.15$ mm K (left panel), 0.75 mm K (center) and 1.95 mm K (right). The broadening of the reconstructed profile is evidently smaller at higher amplitudes a, which result in a higher SNR.

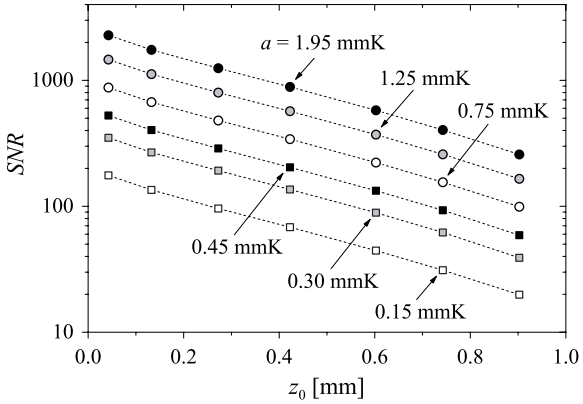

Figure 12. SNR in simulated PPTR signals for δ-functions with different depths z_0 and amplitudes a (see the labels).

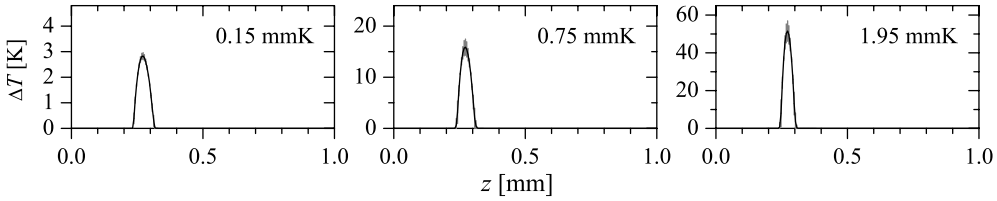

Figure 13. Statistical analysis of 30 temperature profiles reconstructed from simulated PPTR signals corresponding to a δ-profile at $z_0 = 0.273$ mm with the amplitude a varied between 0.15 and 1.95 mm K (see the labels).

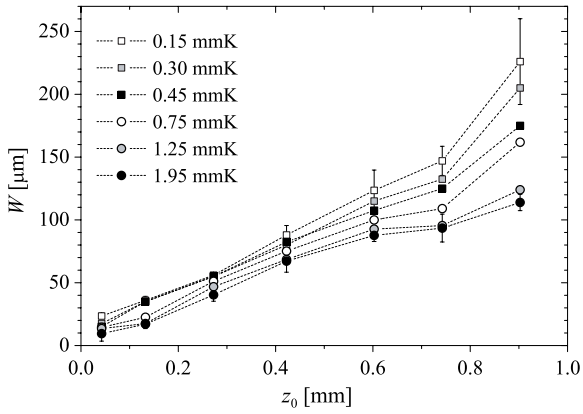

Figure 14. Width W of the reconstructed image of a delta-function profile (10) as a function of its depth z_0 for different amplitudes a (see the legend).

All resulting image widths (W) are presented in figure 14. At large amplitudes ($a >$ 1 mm K), the widths W increase approximately linearly with absorber depth z_0, but the dependence appears more complicated at lower amplitudes. At any given depth z_0, W decreases with increasing amplitude a, but only to a certain level.

Based on these observations, we approximate the broadening effect with a model function

$$w(z_0, a) = p_1 z_0 + \frac{p_2(z_0)}{a}. \tag{11}$$

A good match with the data in figure 14 is found by using an exponential function in the second term, $p_2(z_0) = \alpha + \beta \exp(z_0/\gamma)$, which results in parameter values $p_1 = 0.14 \pm 0.01$, $\alpha = (2.0 \pm 0.4) \times 10^{-3}$ mm^2 K, $\beta = (1.4 \pm 0.7) \times 10^{-4}$ mm^2 K and $\gamma = 0.19 \pm 0.02$ mm. This indicates that, at sufficiently high amplitudes a, the broadening approaches 14% of the absorber depth.

The broadening function w (11) is compared with the actual widths of experimentally and numerically obtained temperature profiles in figure 10 (dashed lines). The amplitude a corresponding to each radiant exposure was obtained as a product of the profile width W and peak temperature value for test sample C (yielding $a = 0.84$, 1.45 and 1.80 mm K for $H =$ 0.24, 0.35 and 0.51 J cm^{-2}, respectively). The plots display the initially linear dependence of broadening w with absorber depth z_0 and the additional exponential component at deeper depths, which is more pronounced at lower radiant exposures. For the relatively thin absorbing layers involved in our study, the obtained image widths W match the predicted broadening w (11) at depths beyond ~0.5 mm. At increasingly shallower absorber depths (e.g., test samples A–C), the broadening becomes comparable and finally smaller than the actual absorbing layer width, and the latter dominates the observed profile width.

5. Discussion

To our knowledge, this study employs for the first time a spectrally composite matrix $\boldsymbol{K}$ in the reconstruction of temperature depth profiles from experimental PPTR signals. This approach was introduced because numerical studies suggested that it could produce temperature profiles with less artifacts as compared to the customary monochromatic approximation, especially in watery tissues with distinct variation of μ_{IR} within the mid-IR spectral range (Majaron *et al* 2002, Majaron and Milanič 2007). When combined with an optimized experimental set-up and image reconstruction code (involving a non-negatively constrained ν-method and adaptive regularization), the assessed depths of absorbing layers in agar tissue phantoms are accurate within the experimental error of our MRI microscopy results (~15 μm), up to the maximal included depth of 0.5 mm (figure 8). In numerical simulation of the procedure, the depths of reconstructed temperature peaks deviate from the actual object depths by less than 1% up to 0.9 mm deep (figure 11). This demonstrates that the PPTR determined depth of a thin absorbing layer can be very accurate, despite the ill-posedness of the inverse problem and presence of noise.

The above results confirm those by Milner *et al* (1996), who reported a good match between the absorber depths in collagen tissue phantoms determined by PPTR profiling and optical low-coherence reflectometry, albeit with occasional differences up to 60 μm at depths under 0.45 mm. In our recent experimental study involving optical coherence tomography, the maximal observed discrepancy was below 20 μm (Milanič *et al* 2007). However, the accuracy of PPTR profiling could not be assessed more accurately, primarily due to non-uniform thickness of the superficial gel layers.

In the present study, involving phantoms with more uniform superficial and absorbing layers, the depths of the latter were also measured using optical microscopy (samples A–G; not presented). We focused the microscope objective (magnification 40×) on the phantom surface and then on the top surface of the absorbing foil. The optical path between the two locations was assessed using the calibrated focusing gauge and corrected for refraction index

of water ($n = 1.33$) to yield the absorbing layer depth. In most samples, the obtained absorber depths matched the results determined by PPTR temperature profiling within the measurement uncertainty (± 20 μm). The larger systematic error observed in a few samples was likely due to shrinking of the agar layers upon dehydration during optical microscopy, also observed in our earlier histology measurements (Milanič *et al* 2007).

Our experimental and numerical results also agree that, within the tested parameter range, the accuracy of depth determination does not vary strongly with absorbing layer depth or applied radiant exposure.

The broadening effect involved in PPTR temperature profiling was reported and discussed before. In numerical and experimental results by Sathyam and Prahl (1997), the broadening effect amounted to 50–60% of the absorber depth Z. Smithies *et al* (1998) estimated the broadening to ~25% of Z, but only in a simulation involving monochromatic PPTR signals without noise. In the present study, we demonstrate temperature peaks as narrow as 14–17% of Z (figures 5 and 6) obtained from spectrally broad experimental PPTR signals.

The observed dependence of the widths W on Z and the profile amplitude is replicated by our detailed numerical simulation, involving spectrally composite PPTR signals and realistic noise (figure 10). Numerical modeling enabled us also to assess the broadening of infinitesimally narrow initial profiles, which amounts to ~0.14 z_0 at reasonably high SNR levels. In as much as mapping between the initial temperature profile and PPTR signals (5) and then back to the reconstructed image is linear, the obtained temperature profile will be a convolution between the actual profile and the δ-broadening function corresponding to specific experimental conditions (e.g., figure 13).

Clearly, the broadening is inherently related to SNR in PPTR signals. When decoupling the influences of the initial temperature profile depth and amplitude on the SNR (figure 12), the effect of the first appears more prominent and universal. Increasing the profile amplitude helps improve the reconstructed image only to a certain point, and primarily for deeper objects (figure 14). Vaguely speaking, the latter effect is significant at an SNR below ~300. The combined result of both effects is approximated by function $w(z_0, a)$ (11).

Since the PPTR reconstruction process conserves energy (Sathyam and Prahl 1997), image broadening leads to reduced temperature values (figures 5 and 9). Based on our results, the discussed profiling technique underestimates the temperature of narrow absorbing layers ($W < 0.15\ z$), which is increasingly more pronounced at larger depths. In order to limit this effect, one should attempt to achieve a reasonably high SNR in PPTR signals.

The present study involved agar tissue phantoms both to enable a direct comparison with earlier reports and for practical reasons. We believe that the demonstrated effects are relevant also for PPTR profiling in human skin, because water is the primary chromophore in the mid-IR spectral region in both tissues. However, the somewhat lower values of μ (due to lower water content in skin) will make the reconstruction problem slightly more ill-posed as compared to the agar gel (Milner *et al* 1995). For this reason, we are currently developing collagen-based tissue phantoms, which resemble more closely the IR-optical and thermal properties of human skin.

In general, chromophores in biological tissues are not organized in planar structures with uniform optical absorption. We selected the described geometry because it enabled us to produce laboratory samples with controlled and repeatable optical properties, which could be accurately replicated in the numerical model. Based on the linearity of (5), superposition principle applies to situations with more complex depth profiles (e.g., Choi *et al* 2004a, Majaron and Milanič 2007). Nevertheless, the demonstrated technique can only be applied to specific tissue structures where the validity of one-dimensional approximation is ensured. One clinically relevant example are port wine stain lesions in human skin, where most

prominent discrete absorbers (melanosomes in the epidermis, venules in papillary dermis) are so numerous and small in comparison with the signal acquisition area (typically several mm^2) that optical absorption can be considered uniform in the lateral direction.

It is also worth noting that the structure-to-data kernel function for the case of three-dimensional photothermal imaging is a product of the customary Green's function, governing heat diffusion parallel to the sample surface and axial kernel function which is exactly the same as $K(z, t)$ in the present study (Nelson *et al* 1996). Because image blurring is much larger in the axial as compared to the lateral direction (Choi *et al* 2004b), any improvement in depth profiling is transferable directly to enhanced photothermal imaging.

6. Conclusions

By employing a spectrally composite matrix in the image reconstruction process, PPTR temperature profiling enables accurate localization of thin absorbing layers in agar tissue phantoms to a depth of at least 0.5 mm. The inherent broadening of reconstructed temperature peaks is reduced to ∼14% of the absorber depth, which is significantly less than that in any earlier experimental realization of this technique.

Acknowledgments

This work was supported by the Slovenian Research Agency (ARRS). The authors thank Nadja Dervišević for sample preparation and laboratory assistance.

References

Bindra R M S, Imhof R E and Eccleston G M 1994 *In vivo* opto-thermal measurement of epidermal thickness *J. Phys. IV* **C7** 445–8

Brakhage H 1987 On ill-posed problems and the method of conjugate gradients *Inverse and Ill-Posed Problems* ed H W Engl and C W Groetsch (London: Academic) pp 165–75

Choi B, Majaron B and Nelson J S 2004a Computational model to evaluate port wine stain depth profiling using pulsed photothermal radiometry *J. Biomed. Opt.* **9** 299–307

Choi B, Majaron B and Nelson J S 2004b Evaluation of photothermal tomography for imaging of microvasculature in human skin *Advanced Biomedical and Clinical Diagnostic Systems II; Proc. SPIE* **5318** 108–112

Cody W J 1969 Rational Chebyshev approximations for the error function *Math. Comput.* **23** 631–8

Girard P A 1989 A fast 'Monte Carlo cross-validation' procedure for large least squares problems with noisy data *Numer. Math.* **56** 1–23

Groetsch C W 1984 *The Theory of Tichonov Regularization for Fredholm Equations of the First Kind* (Marshfield, MA: Pitman)

Hansen P C 1998 *Rank-Deficient and Discrete Ill-Posed Problems* (Philadelphia, PA: SIAM)

Jacques S L, Nelson J S, Wright W H and Milner T E 1993 Pulsed photothermal radiometry of port-wine-stain lesions *Appl. Opt.* **32** 2439–46

Long F H, Anderson R R and Deutch T F 1987 Pulsed photothermal radiometry for depth profiling of layered media *Appl. Phys. Lett.* **51** 2076–8

Majaron B and Milanič M 2007 Re-evaluation of pulsed photothermal radiometric profiling in samples with spectrally varied infrared absorption coefficient *Phys. Med. Biol.* **52** 1089–101

Majaron B and Milanič M 2008 Effective infrared absorption coefficient for photothermal radiometric measurements in biological tissues *Phys. Med. Biol.* **53** 255–68

Majaron B, Verkruysse W, Tanenbaum B S, Milner T E and Nelson J S 2002 Spectral variation of infrared absorption coefficient in pulsed photothermal profiling of biological samples *Phys. Med. Biol.* **47** 1929–46

Majaron B, Verkruysse W, Tanenbaum B S, Milner T E, Telenkov S A, Goodman D M and Nelson J S 2000 Combining two excitation wavelengths for pulsed photothermal profiling of hypervascular lesions in human skin *Phys. Med. Biol.* **45** 1913–22

Milanič M 2008 Development and evaluation of pulsed photothermal radiometry for temperature profiling in biological tissues *PhD Thesis* University of Ljubljana

Milanič M, Majaron B and Nelson J S 2007 Pulsed photothermal temperature profiling of agar tissue phantoms *Lasers Med. Sci.* **22** 279–84

Milanič M, Majaron B and Nelson J S 2008 Spectral filtering for improved pulsed photothermal temperature profiling in agar tissue phantoms *J. Biomed. Opt.* **13** 064002

Milner T E, Goodman D M, Tanenbaum B S and Nelson J S 1995 Depth profiling of laser-heated chromophores in biological tissues by pulsed photothermal radiometry *J. Opt. Soc. Am.* A **12** 1479–88

Milner T E, Smithies D J, Goodman D M, Lau A and Nelson J S 1996 Depth determination of chromophores in human skin by pulsed photothermal radiometry *Appl. Opt.* **35** 3379–85

Nelson J S, Milner T E, Tanenbaum B S, Goodman D M and van Gemert M J C 1996 Infra-red tomography of port-wine stain blood vessels in human skin *Lasers Med. Sci.* **11** 199–204

Sathyam U S and Prahl S A 1997 Limitations in measurement of subsurface temperatures using pulsed photothermal radiometry *J. Biomed. Opt.* **2** 251–61

Smithies D J, Milner T E, Tanenbaum B S, Goodman D M and Nelson J S 1998 Accuracy of subsurface distributions computed from pulsed photothermal radiometry *Phys. Med. Biol.* **43** 2453–63

van Gemert M J C *et al* 1997 Non-invasive determination of port wine stain anatomy and physiology for optimal laser treatment strategies *Phys. Med. Biol.* **42** 937–50

Verkruysse W, Majaron B, Choi B and Nelson J S 2005 Combining singular value decomposition and non-negative constraint in a hybrid method for photothermal depth profiling *Rev. Sci. Instrum.* **76** 024301

Verkruysse W, Majaron B, Tanenbaum B S and Nelson J S 2000 Optimal cryogen spray cooling parameters for pulsed laser treatment of port wine stains *Lasers Surg. Med.* **27** 165–70

Vitkin I A, Wilson B C and Anderson R R 1995 Analysis of layered scattering materials by pulsed photothermal radiometry—application to photon propagation in tissue *Appl. Opt.* **34** 2973–82